

# Morphology of aerosol aggregates formed during co-pyrolysis of $C_3H_8$ + $Fe(CO)_5$

N.A. Ivanova<sup>1</sup>, A.A. Onischuk<sup>1</sup>, S. di Stasio<sup>2</sup>, A.M. Baklanov<sup>1</sup>, G.A. Makhov<sup>1</sup>

<sup>1</sup>Institute of Chemical Kinetics and Combustion SB RAS, 630090, Novosibirsk, Russia

<sup>2</sup>Istituto Motori C.N.R. Aerosol and Nanostructures Laboratory, Via Marconi 8 – 80125, Napoli – Italy

**Abstract.** Formation of aerosol nanoparticles as well as carbon nanotubes and nanofilaments is studied during co-pyrolysis of iron pentacarbonyl and propane with argon as a carrier gas in a flow reactor. Gaseous intermediates from propane thermal decomposition ( $CH_4$ ,  $C_2H_6$  and  $C_3H_4$ ) and  $Fe(CO)_5$  conversion are monitored by Gas Chromatography and by IR-spectroscopy, respectively. The aerosol morphology is studied by Transmission Electron Microscopy (TEM) and High Resolution TEM. The aerosol particle concentration and size distribution are measured by an Automated Diffusion Battery. The crystal phase composition of particles is studied by X-ray diffractometry. The co-pyrolysis of  $Fe(CO)_5$  and  $C_3H_8$  mixed with Ar carrier gas resulted in aerosol aggregate structures dramatically different from those formed by propane pyrolysis. In particular, with the temperature in the range 1070 – 1280 K, we observed  $Fe_3C$  particles connected by long carbon nanotubes (CNTs). The aggregate morphology is described in terms of fractal-like dimension  $D_f$  which is determined from TEM images on the basis of scaling power law linking aggregate mass ( $M$ ) and radius ( $R$ ),  $M \sim R^{D_f}$ . The  $Fe_3C$ -CNT aggregate morphology is a function of the inlet ratio between propane and iron pentacarbonyl concentrations  $[C_3H_8]_0 / [Fe(CO)_5]_0$ . At the low ratio  $[C_3H_8]_0 / [Fe(CO)_5]_0 < 80$  the fractal dimension of aggregates is decreasing (from 1.7 down to about 1) with the inlet concentrations ratio increasing. This effect, as observed by TEM, is due to the increase of mean nanotube length. Vice versa, in the range  $[C_3H_8]_0 / [Fe(CO)_5]_0 > 80$  the fractal aggregate dimension is higher for larger ratio  $[C_3H_8]_0 / [Fe(CO)_5]_0$ , which is explained with the larger thickness of growing nanotubes obtained for relatively large propane concentration. The aggregate formation mechanism includes consecutive stages of iron aggregate formation due to  $Fe(CO)_5$  decomposition, carbon deposition to iron particles from  $C_3H_8$  pyrolysis intermediates; carbon dissolution in iron particles, nanotube nucleation at the carbon concentration of about 60 at.% in Fe-C solution, disruption of the Fe-C aggregates to small pieces by the growing nanotubes.

## 1. Introduction

Pyrolysis and combustion of hydrocarbons are typical soot forming processes. Soot particles are hazardous source of atmospheric pollution [1]. The toxicity of such aerosol particles is related to their size and morphology [2]. In particular, it is known, that the soot chain-like aggregates can adsorb the semivolatile organic compounds more efficiently, than compact aggregates [3]. Soot particles (or aggregates of particles) with size  $\sim 1 \mu m$  can penetrate and remain in the alveolar regions of human lungs resulting in mutagenic and carcinogenic effect [4]. Both the lung penetration and macrophage clearance depend essentially on the aerosol aggregate structure [5]. Thus, the study of morphology of the soot aerosol aggregates formed during the hydrocarbon pyrolysis and combustion is of current importance. Soot aggregate morphology is controlled by different factors such as humidity (which leads to restructuring of aggregates to compact structures [6]), high temperature (which causes soot aggregate restructuring in the flame [7]), electric charge, which can effect the morphology at the stage of cluster-cluster aggregation [8, 9] and govern the aggregate restructuring [10].

Basic flame synthesis and pyrolysis of hydrocarbons can be used in combination with the addition of organometallic precursors (containing Co, Ni, Fe) in order to induce dramatic changes upon the morphology of the generated carbon aerosol nanoparticles. In particular, these routes may be used for synthesis of carbon nanotubes (CNTs) and carbon nanofibers (CNFs) [11-16, 20]. These structures represent a new important class of technological materials that have numerous novel and useful properties [17-19]. The transport properties, coagulation rate constant, specific surface area for this kind of aerosols can change significantly under small variation of the synthesis conditions. During the last decade CNTs and CNFs have come under toxicology scrutiny [21, 22]. The ability of long and thin fibers to reach the gas-exchange region of the lungs gives rise to anxiety of the scientific society. The lung penetration efficiency depends both on length and shape [23]. The CNT and CNF aerosol if inhaled can cause such types of pathology as fibrosis, pleural changes and mesothelioma [22, 24-26] as well as oxidative stress in cells [27-29]. Furthermore, the transition metals used as precursors in hydrocarbon mixture, are included as constituents of the CNT and CNF aerosol and, therefore, may contribute to the oxidative – induced inflammation and toxicity [23].

As a consequence of the points outlined above, it is apparent the relevance of studies concerned with evolution of nanostructure and morphology occurring during the formation of hybrid carbon-metal nanoaerosols.

This work investigates the morphology of aerosol aggregates obtained in a flow reactor by a co-pyrolysis of propane with iron pentacarbonyl diluted in argon which is a typical system for the CNT generation. Besides, the interest to  $\text{Fe}(\text{CO})_5$  is caused by its efficient use as the fire suppressant in the hydrocarbon flames [30, 31].

The objective of this paper is to study the complex topic of aerosol particle formation from the pyrolysis of  $\text{C}_3\text{H}_8 + \text{Fe}(\text{CO})_5$  mixtures, including the eventual changes of aerosol size, nanostructure and morphology occurring during the whole process. This complex phenomenology is comprehensive of understanding the mechanisms of Fe-C aggregate formation and carbon nanotube nucleation ( $\text{C}_3\text{H}_8 + \text{Fe}(\text{CO})_5 + \text{Ar}$  pyrolysis).

## 2. Experimental

A schematic diagram of the experimental apparatus is shown in Fig. 1. The thermal decomposition was carried out at atmospheric pressure in a quartz horizontal flow reactor with inner diameter of 3.0 cm equipped with a coaxial oven. The mixtures of  $\text{Fe}(\text{CO})_5 + \text{Ar}$  and  $\text{C}_3\text{H}_8 + \text{Ar}$  were prepared beforehand and stored in high pressure gas cylinders. The inlet mole fractions of propane and iron pentacarbonyl were varied from 0 to  $7.6 \times 10^{-3}$  and from 0 to  $1.4 \times 10^{-4}$ , respectively. Almost all the experiments were performed at the same value of flow rate. Thus, further in the text, if not mentioned specially, flow rate was  $8 \text{ cm}^3/\text{s}$  at STP. The reactor was operated at temperatures in the range 440 to 1280 K, which corresponded to residence times in the reaction zone  $\tau = 10.5$  to 5.1 s, respectively.

At the exit of reactor both gaseous by-products and aerosol particles were sampled for analysis. The concentrations of CO and  $\text{Fe}(\text{CO})_5$  vapors were measured by IR-spectrometer Bruker Vector 22. Gas Chromatography was used to determine the concentration of gaseous intermediates from propane pyrolysis as well as propane conversion. Identification of species was accomplished by matching the gas-chromatographic retention times to pure gas standards.

The size and morphology of aerosol particles were observed by a transmission electron microscope (TEM) JEM-100SX and a high resolution transmission electron microscope (HR TEM) JEM-2010. The samples for TEM and HR TEM were obtained by thermophoretical precipitation on standard (3 mm diameter) copper grids covered by the polyvinylformvar or carbon support film. Aerosol concentration and size distribution at room temperature were monitored [32-34] by Automated Diffusion Battery (ADB) Spectrometer, coupled with a condensation chamber (CC) and a condensation nucleus counter (CNC). The crystal phase analysis of particles was carried out by URD-63 diffractometer using  $\text{CuK}_\alpha$  radiation. X-ray diffraction (XRD) samples were obtained directly by deposition of aerosol particles onto high efficiency aerosol filter.

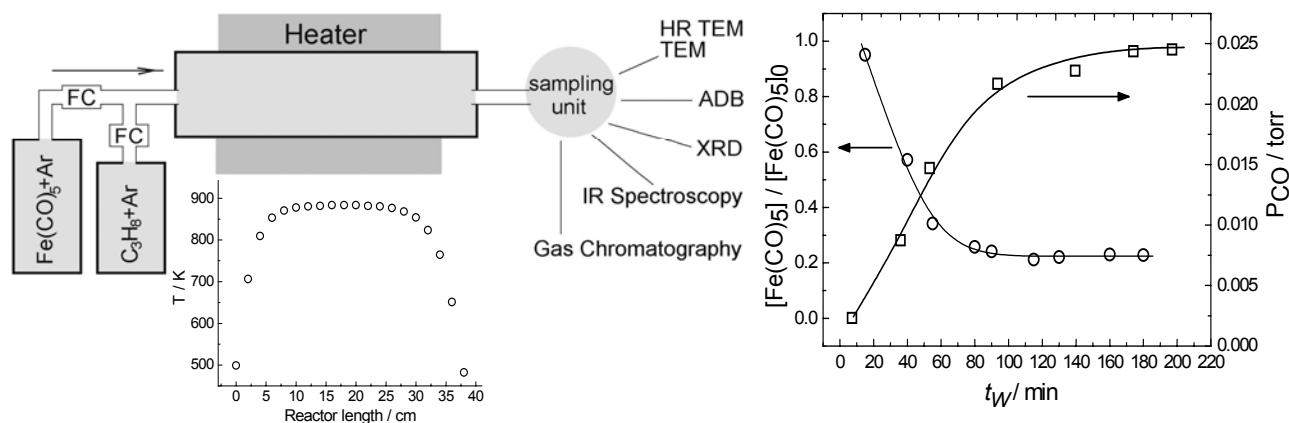


Fig. 1. Schematic diagram of experimental apparatus. FC – flow rate control unit.

Fig. 2. The output  $\text{Fe}(\text{CO})_5$  and CO (right) concentration vs. the laboratory reaction time ( $t_W$ ). Inlet molar fraction is  $[\text{Fe}(\text{CO})_5]_0 = 6.5 \times 10^{-6}$ , pyrolysis temperature  $T = 463 \text{ K}$ .

### 3. Results

#### 3.1. Iron aerosol aggregate formation under $Fe(CO)_5 + Ar$ pyrolysis

The iron pentacarbonyl pyrolysis was carried out as follows. Preliminarily quartz reactor was carefully cleaned. Thereafter, the reaction mixture  $Fe(CO)_5$  plus Ar was supplied at the inlet section of reactor. The outlet concentrations of  $Fe(CO)_5$  and CO (reaction product) were monitored during a few hours of reactor run. The concentration of iron pentacarbonyl  $[Fe(CO)_5]$  was observed to decrease and that of CO to increase, respectively, with respect to increasing of reactor runtime  $t_w$  until both concentrations settle to a stationary level (Fig. 2). This increase of the conversion degree is probably related to the fact that both homogeneous and heterogeneous (wall reaction) decomposition of iron pentacarbonyl occur. The walls are activated during the reaction because of iron deposition resulting to the increase of heterogeneous decomposition rate. In this paper we will consider only the experiments with the activated wall reactor, i.e. when the conversion has come steady to a stationary level.

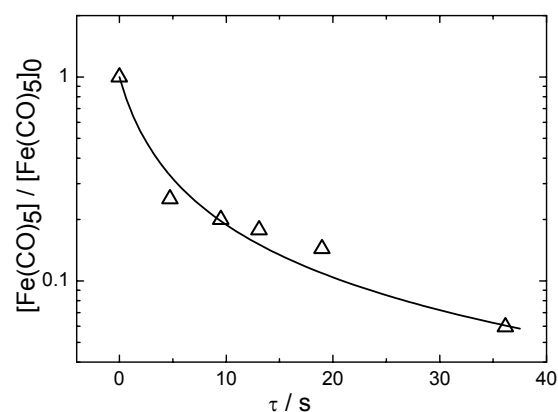


Fig. 3. The output  $Fe(CO)_5$  concentration vs. the residence time ( $\tau$ ). Inlet molar fraction of  $Fe(CO)_5$  is  $6.5 \times 10^{-6}$ , pyrolysis temperature  $T=473$  K.

Fig. 3 shows the conversion of iron pentacarbonyl vs. residence time, which was measured by changing the feeding flow rate at the reactor input. Fig. 4 reports the conversion degree measured as a function of reaction temperature in correspondence of different inlet concentrations  $[Fe(CO)_5]_0$ . These results demonstrate that higher  $[Fe(CO)_5]_0$  do correspond to lower conversion ratio  $[Fe(CO)_5] / [Fe(CO)_5]_0$ .

Aerosol particles collected from reactor outlet on copper grids were observed by TEM. The nature of such aerosol was of aggregates constituted by smaller particles (Fig. 5), which are normally referred in the literature as *primary* particles.

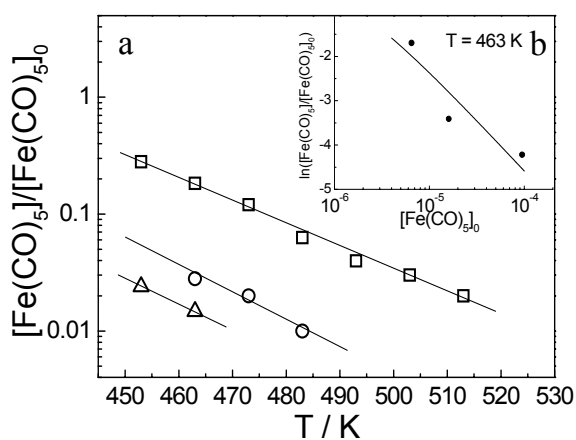


Fig. 4. a. The output  $Fe(CO)_5$  concentration vs. the pyrolysis temperature. Inlet molar fraction of  $Fe(CO)_5$ :  $[Fe(CO)_5]_0 = 6.5 \times 10^{-6}$  (squares),  $1.6 \times 10^{-5}$  (circles) and  $9.5 \times 10^{-5}$  (triangles). Solid lines are eye ball guides. b. The output  $Fe(CO)_5$  relative concentration vs. the inlet  $Fe(CO)_5$  molar fraction for  $T = 463$  K. Solid line corresponds to Eq. 5.

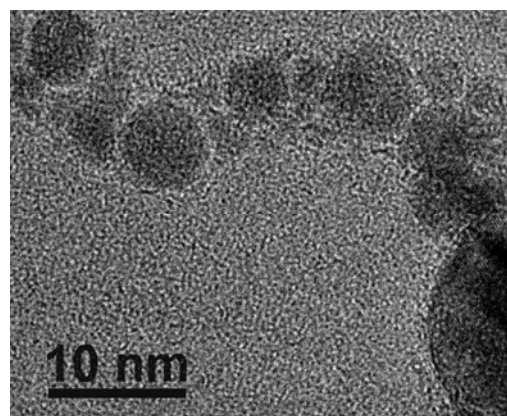


Fig. 5. HR TEM image of iron primary particles inside an aerosol aggregate. Inlet molar fraction is  $[Fe(CO)_5]_0 = 9.5 \times 10^{-5}$ , pyrolysis temperature  $T = 1173$  K.

#### 3.2. Pyrolysis of $C_3H_8 + Ar$ and $C_3H_8 + Fe(CO)_5 + Ar$ mixtures

Figs. 6a-c shows the concentrations of propane and gaseous intermediates at the outlet of the flow reactor as a function of the pyrolysis temperature. It is possible to observe that the gaseous concentrations are almost identical in the two cases of  $C_3H_8 + Ar$  and the  $C_3H_8 + Fe(CO)_5 + Ar$ . Preliminarily pyrolysis of mixture propane plus argon  $C_3H_8 + Ar$  is investigated. This process produces the formation of single spherical soot particles (Fig. 7 a) with typical size spectrum with mode centered about 85 nm as measured by the ADB spectrometer and shown in Fig. 7 b. The size distribution is good described by the log-normal function with the standard geometric deviation  $\sigma_g \approx 1.25$ . Fig. 8 shows the mean arithmetic radius of the soot

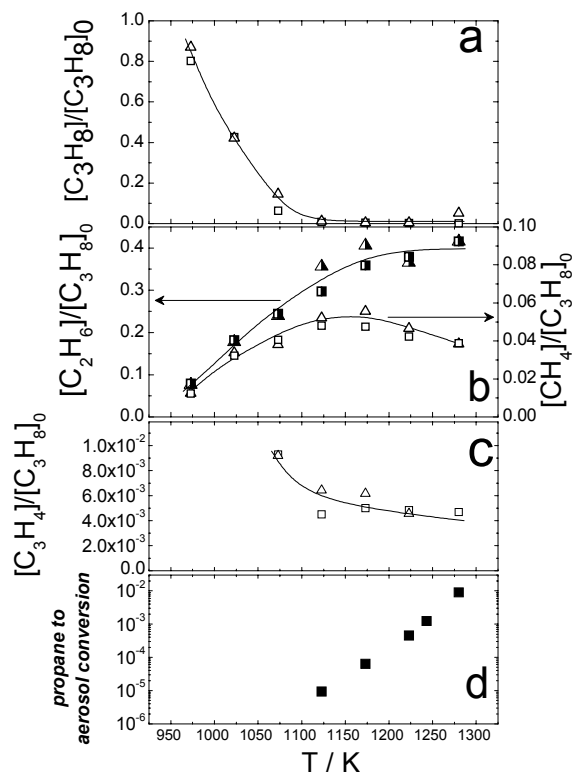


Fig. 6. (a)–(c) The relative gaseous concentrations of propane (a) and intermediates (b, c) in the mixtures sampled at the outlet of reactor vs. the pyrolysis temperature; (d) ratio of the outlet aerosol mass concentration to the inlet mass concentration of carbon to be a constituent of  $C_3H_8$ . Triangular symbols correspond to the Ar +  $C_3H_8$  +  $Fe(CO)_5$  mixture ( $[C_3H_8]_0 = 2.78 \times 10^{-3}$ ,  $[Fe(CO)_5]_0 = 2.8 \times 10^{-5}$ ) and squares – to Ar +  $C_3H_8$  mixture ( $[C_3H_8]_0 = 1.34 \times 10^{-3}$ ).

particles and the particle number concentration at the reactor outlet vs. the temperature of pyrolysis. Both particle radius and concentration are measured to increase with increasing temperature. For comparison, Fig. 8a gives (square) the value of mean particle radius as determined from TEM images elaboration which is in a good agreement with the ADB data (circles). We used the data of Fig. 8 to evaluate the propane to aerosol conversion assuming the particle density to be about  $2 \text{ g/cm}^3$  (see Fig. 6d).

We focus then on the pyrolysis of mixture Ar diluted propane and iron pentacarbonyl. The crystalline structure and morphology of the aggregates formed by the pyrolysis of  $C_3H_8 + Fe(CO)_5 + Ar$  were analyzed by XRD method and TEM, respectively. For the inlet molar fraction ratio  $[C_3H_8]_0 / [Fe(CO)_5]_0$  being in the range from 2 to 40 with  $T = 1173 \text{ K}$  the single crystalline phase  $Fe_3C$  was observed in the XRD patterns (see the example shown above in Fig. 9). The TEM analysis of aggregates produced by pyrolysis of  $C_3H_8 + Fe(CO)_5 + Ar$ , showed that the aggregate morphology was weakly depending upon the initial molar fractions of  $Fe(CO)_5$  and  $C_3H_8$  in the range  $[Fe(CO)_5]_0 = 8.2 \times 10^{-6} - 1.4 \times 10^{-4}$ ,  $[C_3H_8]_0 = 5.2 \times 10^{-4} - 7.6 \times 10^{-3}$  ( $T = 1173 \text{ K}$ ) and was mainly determined by the initial ratio  $[C_3H_8]_0 / [Fe(CO)_5]_0$ . In particular, in correspondence to the range  $[C_3H_8]_0 / [Fe(CO)_5]_0$  below about 30 the aerosol aggregates were observed (Figs. 10 a – c) to be composed by  $Fe_3C$  particles covered by carbon. The diameter of  $Fe_3C$  particles was in the range 5 – 100 nm. Smaller  $Fe_3C$  particles were coated by amorphous carbon (Fig. 10b) whereas graphitized carbon was found to constitute the external shell of larger  $Fe_3C$  particles (Fig. 10c).

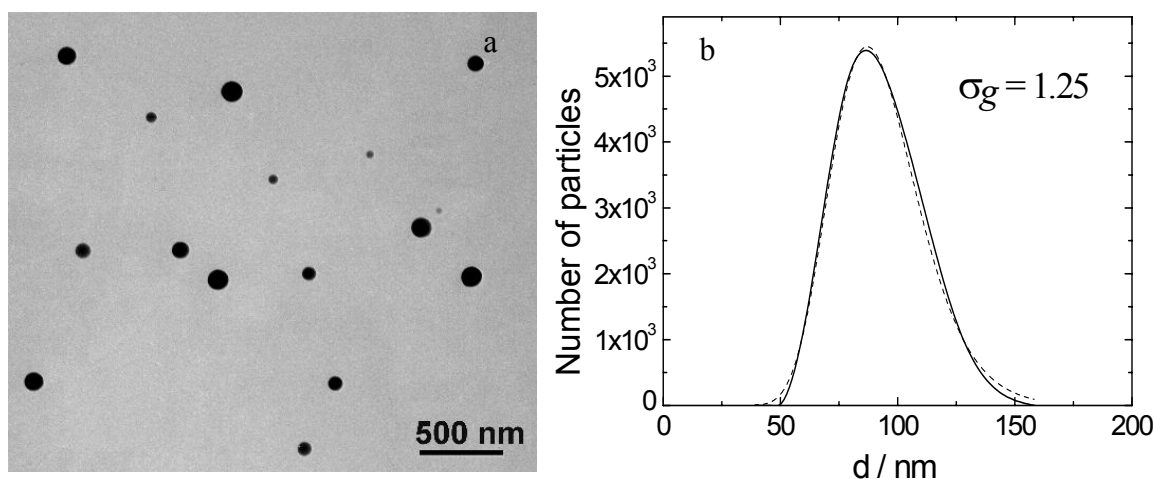


Fig. 7. (a) TEM image and (b) size distribution of soot nanoparticles formed during the pyrolysis of Ar +  $C_3H_8$  mixture at  $T = 1280 \text{ K}$  and inlet molar fraction  $[C_3H_8]_0 = 1.34 \times 10^{-3}$ . Solid line – ADB data; dotted line corresponds to Log-normal function with the standard geometric deviation  $\sigma_g = 1.25$ .

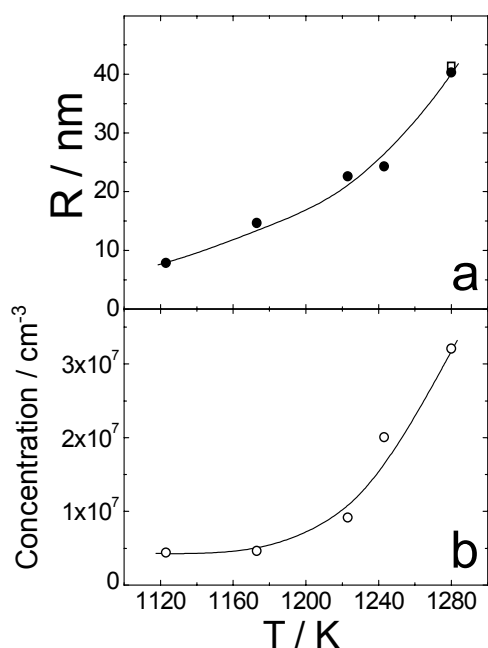


Fig. 8. Mean arithmetic radius  $R$  (a) and number concentration (b) of soot nanoparticles as measured at the outlet of reactor (at room temperature) vs. the pyrolysis temperature, inlet molar fraction is  $[C_3H_8]_0 = 1.34 \times 10^{-3}$  (circles – ADB data, square – TEM data).

aggregate image is proportional to the local thickness of the original aggregate. Therefore, the mass of the original aggregate is considered to be proportional to the integral density of the aggregate image. This approach seems to be reasonable because it is known that even the fractal-like dimension of two-dimensional projection is approximately equal to the  $D_f$  value of the original 3D object if  $D_f < 2$  [35, 36].

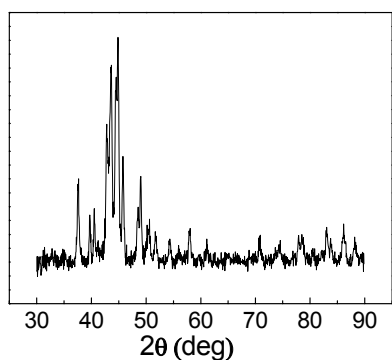


Fig. 9. XRD pattern of the nanoparticles sampled at  $T = 1173$  K during  $Fe(CO)_5 + C_3H_8$  pyrolysis, the inlet molar fractions are  $[Fe(CO)_5]_0 = 1.4 \times 10^{-4}$  and  $[C_3H_8]_0 = 4.6 \times 10^{-3}$ .

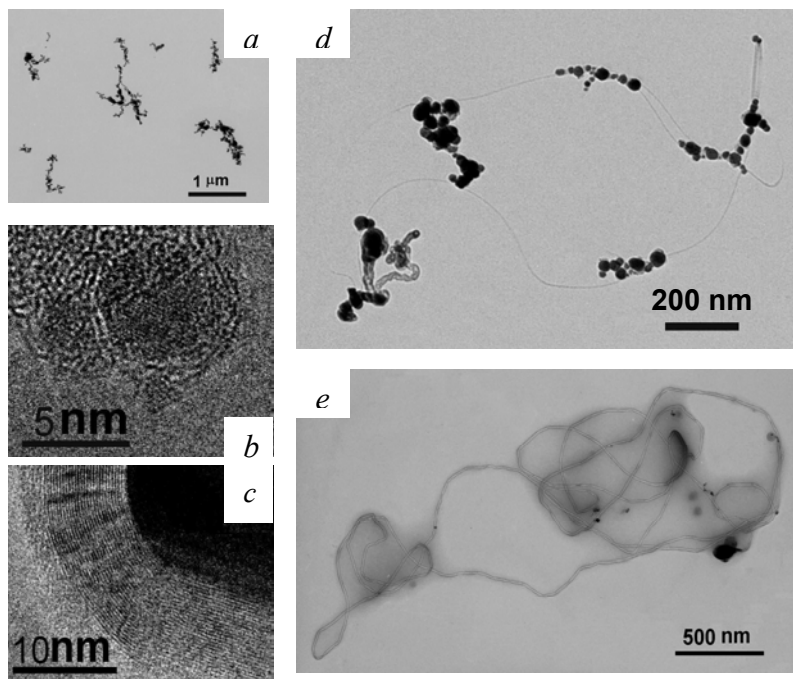


Fig. 10. Examples of TEM and HR TEM images of  $Fe_3C$  covered by carbon (a,b,c) and complex aggregates (d, e) formed under co-pyrolysis of propane and  $Fe(CO)_5$ . Pyrolysis temperature  $T = 1173$  K, inlet molar fractions  $[C_3H_8]_0$  and  $[Fe(CO)_5]_0$  are  $1.25 \times 10^{-3}$  and  $1.052 \times 10^{-4}$  (a,b,c) and  $7.5 \times 10^{-4}$  and  $9.2 \times 10^{-6}$  (d),  $5.8 \times 10^{-3}$  и  $9.2 \times 10^{-6}$  (e), respectively. b: small  $Fe_3C$  particles of aggregate covered by amorphous carbon shell; c: large  $Fe_3C$  particle of aggregate coated by graphite-like shell.

In the range  $[C_3H_8]_0 / [Fe(CO)_5]_0 > 30$  carbon nanotubes were formed, thus, the resulted structures consisted of small groups particles, connected by long single wall and multi wall nanotubes (Fig. 10d,e). The length and diameter of carbon nanotubes depended on the inlet mixture composition and pyrolysis temperature. For example, the typical conditions of carbon nanotube formation were the temperature range  $1073 < T < 1280$  K and the ratio of reagent concentrations  $30 < [C_3H_8]_0 / [Fe(CO)_5]_0 < 650$ . Fig. 11 shows the mean arithmetic diameter and length of carbon nanotubes vs. the inlet propane to iron pentacarbonyl ratio of molar fractions. The mean diameter and the length of carbon nanotubes increase with the ratio  $[C_3H_8]_0 / [Fe(CO)_5]_0$ . Results from TEM analysis were compared with some findings from HRTEM (square point in Fig. 11b) in order to check for reliability of assessment of CNT mean arithmetic diameter. Accord was found and most of analysis was performed on TEM observations. We used the fractal-like dimension ( $D_f$ ) approach to describe the morphology of complex aggregates composed by both particles and nanotubes using relationship [35]:

$$M \propto R^{D_f} \quad (1),$$

where  $M$  - aggregate mass,  $R$  - radius.

To determine the mass  $M$  of each aggregate we measure the integral density of individual aggregate as the sum of the gray values of all the pixels which constituted the aggregate image. A correction to the background density was also done. It is assumed that the local gray density in the

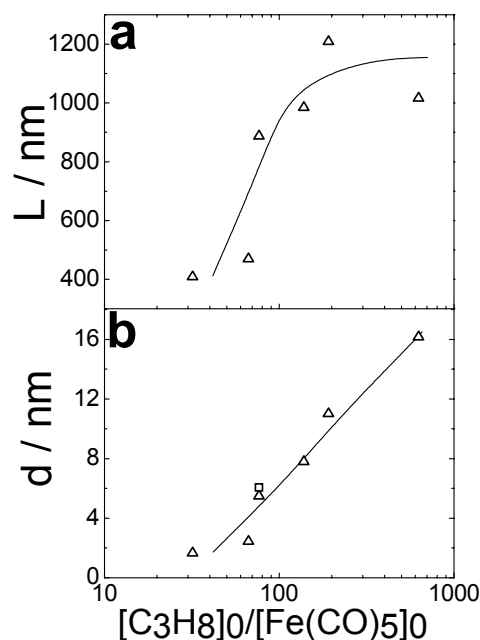


Fig. 11. Mean arithmetic length ( $L$ ) and diameter ( $d$ ) of carbon nanotubes vs. the ratio of inlet molar fraction  $[C_3H_8]_0/[Fe(CO)_5]_0$ , pyrolysis temperature  $T=1173$  K (triangles – TEM image elaboration, square symbol – data of HR TEM).

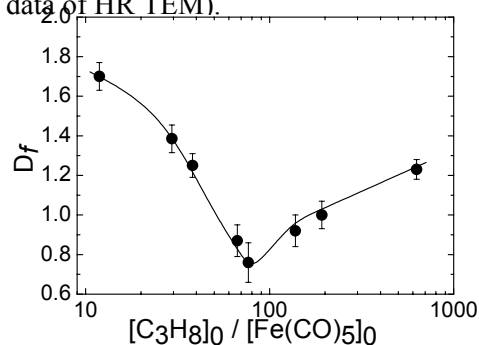


Fig. 12. Dependence of fractal-like dimension complex aggregates on the inlet ratio  $[C_3H_8]_0/[Fe(CO)_5]_0$ ; pyrolysis temperature  $T = 1173$  K.

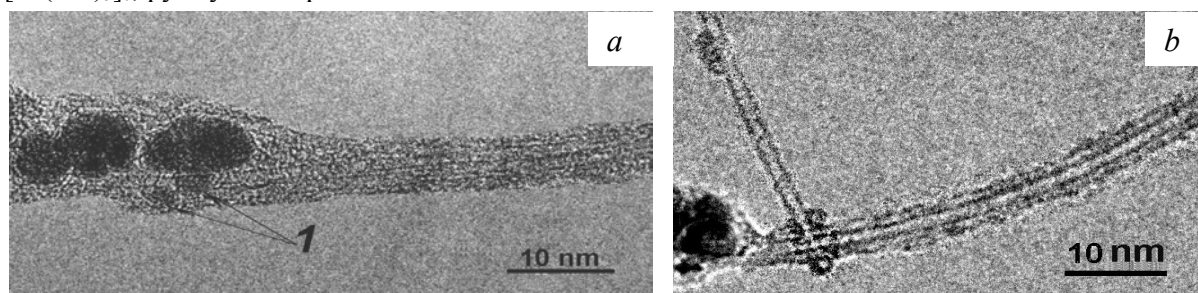


Fig. 13. HR TEM images of single-wall carbon nanotubes (SWNTs) formed by pyrolysis of  $C_3H_8 + Fe(CO)_5 + Ar$  mixture ((a)) – $Fe_3C$  nanoparticles on basis of SWNTs. Pyrolysis temperature  $T=1173$  K, inlet molar fractions of reagents  $[C_3H_8]_0$  and  $[Fe(CO)_5]_0$  are  $7.5 \times 10^{-4}$  and  $9.2 \times 10^{-6}$ , respectively.

## 4. Discussion

### 4.1. Pyrolysis of $Fe(CO)_5 + Ar$ mixture

It is important to know the temperature region in which the homogeneous decomposition dominates. The pentacarbonyl homogeneous decomposition can be described by the first order kinetics via the expression:

The geometric radius was determined from TEM images according to a procedure described in detail elsewhere [37] from the following equation:

$$R = \frac{1}{2} \sqrt{LW}, \quad (2)$$

where  $L$  and  $W$  are the dimensions of the smallest rectangle enclosing the 2D image of the aggregate.

Fig. 12 shows  $D_f$  vs. the  $[C_3H_8]_0/[Fe(CO)_5]_0$  ratio.  $D_f$  is observed to be decreasing upon increasing the ratio  $[C_3H_8]_0/[Fe(CO)_5]_0$  from about 10 up to 80. This result is coherent with the finding discussed above about the increase of the mean nanotube length with propane relative concentration (Fig. 11a). At higher ratios ( $[C_3H_8]_0/[Fe(CO)_5]_0 > 80$ ) the fractal-like dimension increases with increasing  $[C_3H_8]_0/[Fe(CO)_5]_0$  ratio. This result is in an agreement with the fact that the mean nanotube length does not change with propane relative concentration in this range, whereas the mean nanotube diameter increases monotonically (Fig. 11 b). HR TEM analysis showed the complex aggregates contain different kind nanotubes including single-wall (Fig. 13) as well as multi-wall nanotubes (Figs. 14, 15). At low ratios  $[C_3H_8]_0/[Fe(CO)_5]_0 < 80$  single wall nanotubes (SWNT) dominated in the samples; in the range  $80 < [C_3H_8]_0/[Fe(CO)_5]_0 < 140$  both SWNTs and bamboo-like nanotubes were present. At  $[C_3H_8]_0/[Fe(CO)_5]_0 > 150$  the samples contained both bamboo-like and hollow MWNTs.

From TEM images it is possible to evaluate the fraction of nanotubes, i.e. the average number of nanotubes per aggregate, as a ratio between total number of nanotubes and the total number of aggregates in the sample. Actually, this ratio reflects the probability of nanotube nucleation during the reaction time. Fig. 16a shows the nanotube fraction vs. the ratio between the initial concentrations of  $C_3H_8$  and  $Fe(CO)_5$ . One can see, that at  $[C_3H_8]_0/[Fe(CO)_5]_0 > 100$  the nanotube fraction is higher than unity, i.e. many aggregates are observed, which include more than one nanotube.

$$\frac{\Delta[Fe(CO)_5]_{HOM}}{[Fe(CO)_5]_0} = 1 - \exp(-k_{HOM}t) \quad (3)$$

where  $\Delta[Fe(CO)_5]_{HOM}$  represents the decreasing of the iron pentacarbonyl concentration due to the homogeneous decomposition,  $t$  is reaction time,  $k_{HOM}$  is homogeneous decomposition rate constant [38]:

$$k_{HOM} = 5.01 \times 10^{15} \exp(-165458 \pm 9977 \text{ (J/mol)/RT}) \text{ (s}^{-1}\text{)} \quad (4)$$

The solid line in Fig. 17 shows the prediction of iron pentacarbonyl decomposition degree at the reactor outlet in the case that only the homogeneous decomposition contributes. The prediction of homogeneous decomposition is considerable at temperature  $T > 500$  K.

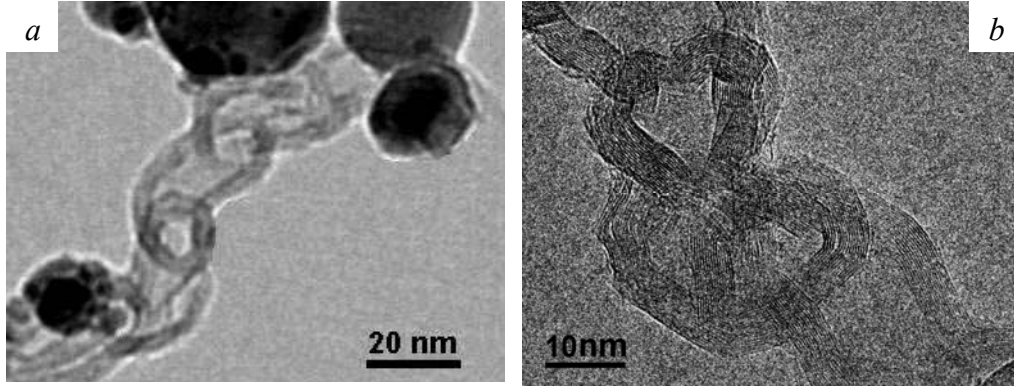


Fig. 14. HR TEM images of bamboo-like multi-wall carbon nanotubes (MWNTs). Pyrolysis temperature  $T=1173$  K, inlet molar fractions of reagents  $[C_3H_8]_0$  and  $[Fe(CO)_5]_0$  are  $7.5 \times 10^{-4}$  and  $9.2 \times 10^{-6}$ , respectively.

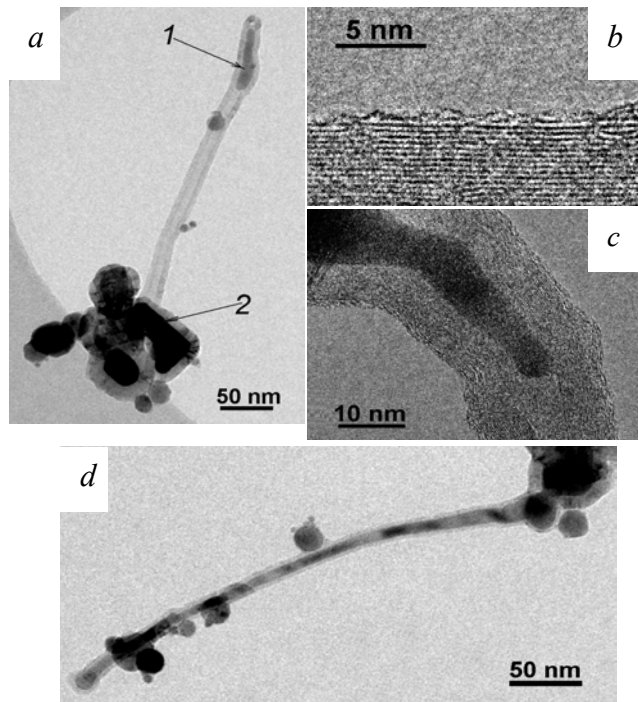
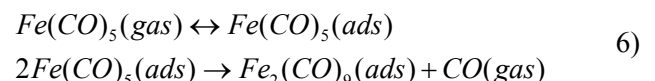


Fig. 15. HR TEM images of multi-wall carbon nanotubes (MWNTs): (a) – an example of hollow MWNT (1- drop-like particle, 2- particle on nanotube basis); (b) – graphite layers of MWNT wall with a lattice parameter ( $d_{002}$ ) 0.34 nm; (c) - nanotube fragment with  $Fe_3C$  drop-like particle; (d) – MWNT thick with  $Fe_3C$ . Pyrolysis temperature  $T=1173$  K, inlet molar fractions  $[C_3H_8]_0$  and  $[Fe(CO)_5]_0$  are  $7.5 \times 10^{-4}$  and  $9.2 \times 10^{-6}$ , respectively.

Results summarized in Figs. 2-4 are now discussed in order to compare the contribute of predicted homogeneous versus measured heterogeneous decomposition. In particular, from Fig.2 in correspondence of lower ( $T < 500$  K) pyrolysis temperatures, the heterogeneous decomposition is found to dominate (see Fig. 2 which shows that the activated wall conversion is about 75% while that for non-activated walls is negligible) and the stationary ratio  $[Fe(CO)_5] / [Fe(CO)_5]_0$  decreases with the inlet  $[Fe(CO)_5]$  concentration increasing with temperature being kept constant (Fig. 4b). We found that the heterogeneous decomposition follows the second order kinetics:

$$\frac{[Fe(CO)_5]}{[Fe(CO)_5]_0} = (1 + k[Fe(CO)_5]_0 t)^{-1}, \quad (5)$$

where  $k$  is the second order rate constant (see, Fig. 4b and Fig. 3). From the data shown in Fig. 3 the rate constant was determined  $k = 4.2 \times 10^{-15} \text{ cm}^3 \text{ s}^{-1}$ . It is reasonable to assume that the limiting stage is the surface dimerization:



The total  $Fe(CO)_5$  conversion (as follows from Fig. 4) is presented in Fig. 17 with sphere symbols. It is interesting to compare the total conversion with the homogeneous decomposition degree and the efficiency  $\alpha$  of conversion of  $Fe(CO)_5$  to the aerosol particles. The efficiency  $\alpha$  can be evaluated as the ratio between the outlet aerosol mass concentration

and the inlet mass concentration of Fe which is a constituent of  $\text{Fe}(\text{CO})_5$ . We evaluated the outlet aerosol mass concentration from the temperature dependencies of aerosol number concentration (ADB data) and radius using Eq. (2). In the temperature range  $T = 450 - 490$  K the aerosol conversion is approximately equal to the homogeneous decomposition degree which means that aerosol particles are a product of homogeneous decomposition. At the pyrolysis temperature higher than 500 K aerosol conversion does not exceed 0.30 which is much less than the  $\text{Fe}(\text{CO})_5$  homogeneous decomposition degree. The discrepancy may be related to the heterogeneous loss of  $\text{Fe}(\text{CO})_5$  in the preheating zone (i.e. the inlet zone at the range 0 – 5 cm, see, Fig. 1).

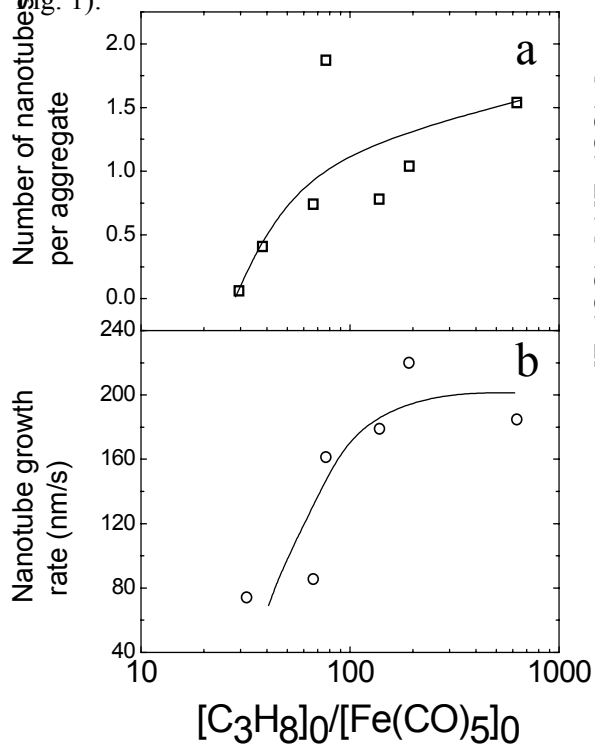


Fig. 16. The number of nanotubes per aggregate (a) and nanotube growth rate (b) as a function of the inlet ratio  $[\text{C}_3\text{H}_8]_0 / [\text{Fe}(\text{CO})_5]_0$ ; pyrolysis temperature  $T = 1173$  K

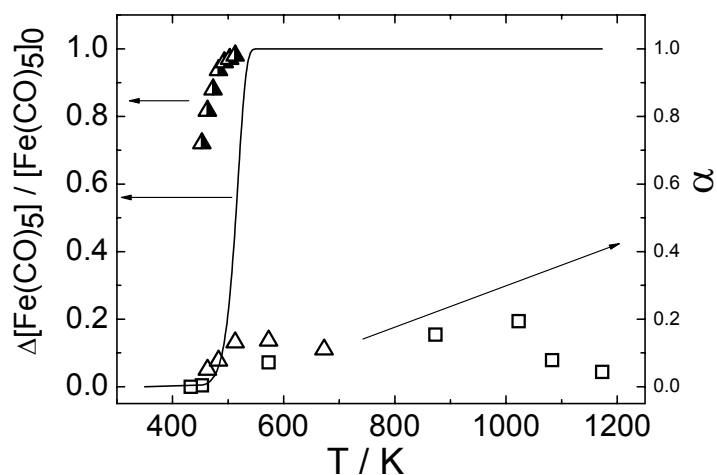


Fig. 17. Temperature dependence of the iron pentacarbonyl decomposition degree and the ratio ( $\alpha$ ) of the outlet aerosol mass concentration to the iron mass concentration to be a consistent of the inlet  $\text{Fe}(\text{CO})_5$ . Solid line was calculated via Eqs (4, 5). Semi-filled symbols – experimental data. Open symbols – evaluations from the values of aerosol number concentration and radius (see text). Inlet molar fractions  $[\text{Fe}(\text{CO})_5]_0 = 6.5 \times 10^{-6}$  (triangles),  $9.5 \times 10^{-5}$  (squares).

#### 4.2. Co-pyrolysis of $\text{C}_3\text{H}_8 + \text{Fe}(\text{CO})_5$ mixtures

Morphology evolution of complex aerosol aggregates has more complicated character, with respect to the case of iron aerosol aggregates. Initial stages of aerosol formation depend essentially on the kinetics of the  $\text{Fe}(\text{CO})_5$  and propane decomposition. We can estimate the decomposition rate of these reagents in our experimental conditions. The rate constant of propane homogeneous decomposition was measured experimentally by different experimental groups for the typical propane pressures to be in the range 0.1 – 1 Bar. These experimental constants are in a good concordance each with the other [39 - 45]. The largest temperature range 1100 – 1400 K was covered by Benson [39] by the shock tube technique resulting to the first order rate constant expression:

$$k_{\text{C}_3\text{H}_8}^{\text{Benson}} = 1.27 \times 10^{12} \exp\left(\frac{-234.5 \text{ kJ/Mole}}{RT}\right) \text{ (s}^{-1}\text{)} \quad (7)$$

Our measurements of this rate constant were done for the inlet propane pressure  $1.1 \times 10^{-3}$  bar, i.e. two orders of magnitude less than in the other authors studies [39 – 45]. Thus, from the experimental data about propane decomposition, see Fig. 11 a, it is possible to infer the following first order rate constant:

$$k_{\text{C}_3\text{H}_8} = 9.13 \times 10^{10} \exp\left(\frac{-233.3 \text{ (kJ/Mole)}}{RT}\right) \text{ (s}^{-1}\text{)} \quad (8)$$

which is an order of magnitude less than the Benson's value. At the pyrolysis temperature  $T = 1073$  K the rate constants for  $\text{Fe}(\text{CO})_5$  and propane decomposition estimated via Eqs. (5, 9) are  $4.4 \times 10^7$  and  $0.4 \text{ s}^{-1}$ , respectively. In other words, in our temperature range the  $\text{Fe}(\text{CO})_5$  decomposition rate was much higher than the propane decomposition rate. Thus, simple estimations show, that the complete decomposition of  $\text{Fe}(\text{CO})_5$  occurs at the reactor input zone on reaching the temperature of about 500 K, while the propane begins to decompose later at 960 K (Fig. 6).

In order to draw a scheme to describe the process occurring in the flow reactor vs. the residence time, in Fig. 18 are shown the gas temperature and the concentrations of  $\text{Fe}(\text{CO})_5$  and  $\text{C}_3\text{H}_8$  as the reacting gases proceed inside the flow reactor (Fig. 18). The initial time corresponds to the reactor inlet point.

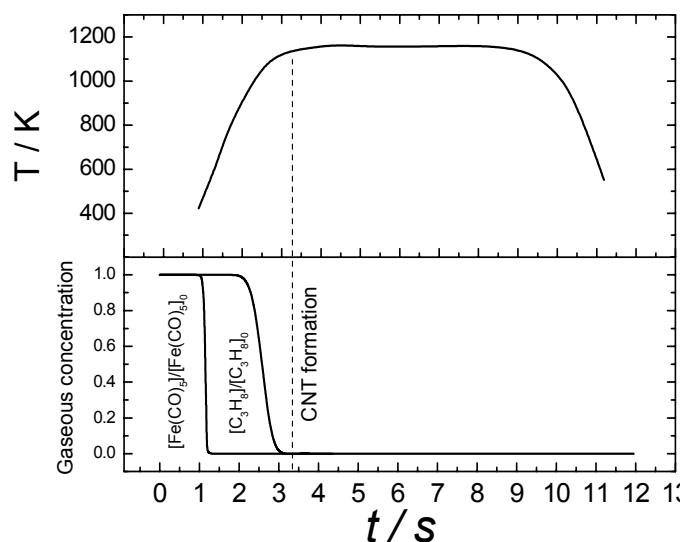


Fig. 18. Scheme of particle evolution during pyrolysis of  $\text{Fe}(\text{CO})_5 + \text{C}_3\text{H}_8 + \text{Ar}$  mixture at reaction temperature 1173 K and input flow rate 8 sccs.

The time-dependence of the gas temperature was recalculated from the experimental temperature profile (see, for example, Fig. 1) taking into account the gas temperature expansion coefficient. The gas concentration curves were calculated from Eqs. (4, 8). One can see that during the time 0 – 1.2 s iron pentacarbonyl decomposes completely, while the propane conversion is negligible. Thus, in the range 1.2 – 2.0 s the flow contains chain-like iron aggregates. During the time 2.0 – 3.0 s propane decomposition occurs at the temperature range 900 – 1120 K. The decomposition is accompanied by the intermediates deposition to the Fe aggregate surface followed by the carbon diffusion to the iron particles. The diffusion process results to the formation of Fe-C solution [46, 47, 49]. The melting point for this solution is about 910 K [46-48], thus, actually, at  $t > 2$  s

the gas flow contains the liquid phase Fe-C particles.

At the reaction time  $t \approx 3.4$  s the carbon concentration reaches a critical value [47] which we estimated (see next paragraph) to be equal to 60 at. %. In correspondence of this critical concentration of carbon the nanotubes nucleation starts [49] (nucleation probability at this moment is about 0.1 for the initial ratio  $[\text{Fe}(\text{CO})_5]_0 / [\text{C}_3\text{H}_8]_0 = 100$ ). The carbon concentration in Fe-C solution was estimated from TEM and HR TEM images in the assumption that in the reactor hot zone the majority of carbon atoms in the aggregates are constituents of the Fe-C solution phase. At the reactor outlet the  $\text{Fe}_3\text{C}$  phase is formed and the excess of carbon forms the graphite or amorphous shell [47]. The estimation of total carbon content in sampled aerosol aggregates was provided by measuring the volumes of carbon shells and  $\text{Fe}_3\text{C}$  particles using the densities for carbon and  $\text{Fe}_3\text{C}$   $\rho_{\text{C}} = 2.0 \text{ g/cm}^3$  and  $\rho_{\text{Fe}_3\text{C}} = 7.7 \text{ g/cm}^3$ . Our estimations of the carbon critical concentration are in reasonable agreement with the experimental observations of the carbon concentration in the liquid Fe-C particles to be 50 at. % at  $T = 910 - 970 \text{ K}$  [46-48]. At time  $t > 3.4$  s both single wall and multi wall nanotubes grow, while liquid Fe-C solution penetrates inside the MWNs (see Fig. 15 a, c, d). The growth of nanotubes has the effect to disrupt the Fe-C aggregates resulting in small Fe-C fragments connected by relatively long nanotubes segments (Fig. 10 d, e).

## 5. Conclusions

In the case of pyrolysis of  $\text{C}_3\text{H}_8 + \text{Ar}$  and  $\text{C}_3\text{H}_8 + \text{Fe}(\text{CO})_5 + \text{Ar}$  mixtures the propane decomposition rate constant was experimentally determined as  $k_{\text{C}_3\text{H}_8} = 9.13 \times 10^{10} \exp(-233.3(\text{kJ/Mole})/RT) (\text{s}^{-1})$ , which signifies an order of magnitude less than the literature data. This discrepancy is probable related to the fact that the propane concentrations used in this work were two orders of magnitude less with respect to other literature studies.

It was found that in the case of  $\text{C}_3\text{H}_8 + \text{Fe}(\text{CO})_5 + \text{Ar}$  mixture pyrolysis complex aggregates composed of  $\text{Fe}_3\text{C}$  particles connected by long nanotubes are formed. The aggregate morphology is a function of the inlet  $[\text{C}_3\text{H}_8]_0 / [\text{Fe}(\text{CO})_5]_0$  ratio. In the range  $10 < [\text{C}_3\text{H}_8]_0 / [\text{Fe}(\text{CO})_5]_0 < 80$ , the aggregate fractal dimension  $D_f$  decreases from 1.7 to 0.8 with  $[\text{C}_3\text{H}_8]_0 / [\text{Fe}(\text{CO})_5]_0$  decreasing, which is related to the increase of the nanotube mean length. Vice versa, in correspondence of increasing  $[\text{C}_3\text{H}_8]_0 / [\text{Fe}(\text{CO})_5]_0$  ratio above 80, aggregate fractal dimension  $D_f$  is observed to rise up again, which can be interpreted as the net result of the increase of the nanotube mean diameter corresponding to a relatively larger propane concentration.

## Acknowledgements

Financial support for this work was provided by the Presidium of Russian Academy of Sciences (project no 78), the Russian Foundation for Basic Research (RFBR) (project nos 07-03-00643a, 05-03-90576-NSC-a) and the NSC(Taiwan)-RFBR no 94WFA0600016 (contract no RP05E15).

## References

1. Longwell J P 1982 *Proceedings of the 19<sup>th</sup> Symposium (International) on Combustion, The Combustion Institute, Pittsburg* 1339
2. Zimmer A T 2002 *J. Environ. Monit.* **4** 628
3. Goss K-U, Eisenreich S J 1997 *Atmospheric Environment* **31** 2827
4. Koshland C P 1996 *Proceedings of the 26th Symposium (International) on Combustion, The Combustion Institute, Pittsburg* 2049
5. Nemmar A, Hoet P H M and Vanquickenborne B 2002 *Circulation* **105** 411
6. Colbeck I, Appleby L, Hardman E J, Harrison R M 1990 *J. Aer. Sci.* **21** 527
7. di Stasio S 2001 *J. Aer. Sci.* **21** 509
8. Richter R, Sander L M, Cheng Z 1984 *J. of Col. and Int. Sci.* **100(1)** 203
9. Hurd A J, Flower W L 1988 *J. of Col. and Int. Sci.* **122** 178-192
10. Onischuk A A, di Stasio S, Karasev V V, et al. 2003 *J. Aer. Sci.* **34** 383
11. Vander Wal R L, Hall L J 2001 *Chem. Phys. Lett.* **349** 178
12. Vander Wal R L, Ticich T M 2001 *Chem. Phys. Lett.* **336** 24
13. Vander Wal R L, Ticich T M, Curtis V E 2000 *Chem. Phys. Lett.* **323** 217
14. Le Q T, Schouler M C, Garden J, Gadelle P 1999 *Carbon* **37** 505
15. Glerup M, Kanzow H, Almairac R, Castignolles M, Bernier P 2003 *Chem. Phys. Lett.* **377** 293
16. Bladh K, Falk L K L, Rohmund F 2000 *Appl. Phys. A: Materials Sci. & Processing* **70** 317
17. Carbon Nanotubes: Synthesis, Structure, Properties, and Applications, edited by Dresselhaus M, Dresselhaus G and Avouris P 2000 Springer-Verlag.
18. Bernholc J, Brenner D, Buongiorno Nardelli M, Meunier V and Roland C 2002 *Annual Review of Materials Research* **32** 347
19. Dresselhaus M S, Dresselhaus G and Jorio A 2004 *Annual Review of Materials Research* **34** 247
20. Awasthi K, Srivastava A, Srivastava O N 2005 *J Nanosci Nanotechnol.* **5** 1616
21. Lam C-W, James J T, McCluskey R and Hunter R 2004 *Toxicol. Sci.* **77** 126
22. Maynard A D, Baron P A, Shvedova A A., Kisin E R and Catranva V 2004 *J. Toxicol. and Environmental Health* **67** 87.
23. Donaldson K, Aitken R, Tran L, Stone V, Duffin R, Forrest G, Alexander A 2006 *Toxicol. Sci.* **92(1)** 5
24. Shvedova A A, Kisin E R, Mercer R, Murray A R, Johnson V J, Potapovich A I, et al. 2005 *Am J Physiol Lung Cell Mol Physiol.* **289(5)** L698
25. Warheit D B, Laurence B R, Reed K L, Roach D H, Reynolds G A, Webb T R 2004 *Toxicol. Sci.*, **77** 117
26. Jia G, Wang H, Yan L, Wang X, Pei R, Yan T, et al. 2005 *Environ Sci Technol.* **39** 1378
27. Monteiro-Riviere N A, Nemanich R J, Inman A O, Wang Y Y and Riviere J E 2005 *Toxicol. Lett.* **155(3)** 377
28. Bottini M, Bruckner S, Nika K, Bottini N, Bellucci S, Magrini A, Bergamaschi A and Mustelin T 2006 *Toxicology Letters* **160(2)** 121
29. Manna S K, Sarkar S, Barr J, Wise K, Barrera E V, Jejelowo O, Rice-Ficht A C, Ramesh G T. 2005 *Nano Lett.* **5(9)** 1676
30. Rummung M D, Reinelt D, Babushok V, and Linteris G T 1999 *Combustion and Flames* **116** (1/2) 207
31. Reinelt D, and Linteris G T 1996 *26-th Symposium (International) on Combustion, The Combustion Institute* 1421
32. Mavliev R A, Ankilov A N 1985 *Colloidny journal (Russ.)* **15(3)** 523
33. Mavliev R A, Ankilov A N, Baklanov A M 1984 *Colloidny journal (Russ.)* **46(6)** 1136
34. Ankilov A, Baklanov A, Mavliev R, Eremenko S 1991 *J. Aer. Sci.* **22** S325
35. Friedlander S K 2000 *Smoke, dust and haze. New York, Oxford: Oxford University Press*
36. Rogak S N, Baltensperger U, Flagan R C 1991 *Aer. Sci. and Tech.* **14** 447
37. Samson R J, Mulholland G W, Gentry J W 1987 *Langmuir* **3** 272
38. Lewis K E, Golden D M, Smith G P 1984 *J. Am. Chem. Soc.* **106** 3905
39. Benson A M 1967 *AIChE J.* **13** 903
40. Bakh G; Novak Z, Korochuk S I, Kalinenko R A 1974 *Kinet. Catal.* **15** 1103
41. Zychlinski W, Bach G, Heinrich K, Zimmermann G 1979 *Chem. Tech. (Leipzig)* **31** 1191
42. Kalinenko R A, Buravtseva E N, Nametkin N S et al. 1983 *Kinet. Catal.* **24** 1031
43. Laidler K J, Sagert N H, Wojciechowski B W 1962 *Proc. R. Soc. London* **270** 254
44. Jezequel J Y, Baronnet F, Niclaude M 1983 *J. Chim. Phys.* **80** 455
45. Marek L F, Cluer W B 1931 *Ind. Eng. Chem.* **23** 878

46. Krivoruchko O P, Maksimova N I, Zaikovski V I, Salanov A N 2000 *Carbon* **38** 1075
47. Krivoruchko O P, Zaikovski V I 1998 *Kinet. Catal.* **39(4)** 607
48. Parmon V N 1996 *Catal. Lett.* **42** 195
49. Maksimova N I, Krivoruchko O P, Mestl G, Zaikovskii V I, Chuvilin A L, Salanov A N, Burgina E B 2000 *J. of Molecular Catalysis A: Chemical* **158** 301